Temperature-induced stress relaxation in alloyed silver-gold nanoparticles (7 to 8 nm) by *in-situ* X-ray powder diffraction

*Oleg Prymak[1], Viktoria Grasmik[1], Kateryna Loza[1], Marc Heggen[2], Matthias Epple[1]**

[1] Inorganic Chemistry and Center for Nanointegration Duisburg-Essen (CeNIDE), University of Duisburg-Essen, Universitätsstr. 5-7, 45117 Essen, Germany

[2] Ernst Ruska-Centre for Microscopy and Spectroscopy with Electrons, Forschungszentrum Jülich GmbH, 52425 Jülich, Germany

KEYWORDS Silver, gold, alloys, nanoparticles, X-ray diffraction, *in-situ*

ABSTRACT Alloyed silver-gold nanoparticles (spherical, 8 nm) were wet-chemically prepared by reduction with sodium citrate/tannic acid and colloidally stabilized by poly(N-vinylpyrrolidone), PVP, in steps of 10 at%, including pure silver nanoparticles (35 nm) and pure gold nanoparticles (7 nm). The nanoparticles were subjected to *in-situ* X-ray powder diffraction up to 850 °C to induce internal stress relaxation and recrystallization. The stress-induced negative deviation from Vegard's rule that was present in the original alloyed nanoparticles vanished between 150 and 250 °C, indicating the internal healing of defects. Simultaneously, a

discontinuous increase in the crystallite size and a drop in the microstrain were observed. After heating to 850 °C, the original gradient structure (silver-rich shell, gold-rich core) had changed to a homogeneous elemental distribution as shown by high-angle annular dark-field STEM/EDX. Thus, there is a considerable mobility of the metal atoms inside the nanoparticles that starts as low as 150 °C.

Introduction

Silver and gold nanostructured materials (e.g. particles or coatings) are among the most prominent metals in industry and biomedicine due to the antibacterial effect of silver, their easy functionalization, e.g. by thiol or phosphane chemistry, and their plasmonic effects which are useful for imaging.[1-11] Alloying both metals in one nanoparticle allows to fine-tune their element-specific physicochemical and biological properties.[2, 3, 12-14]

Crystallizing in a face-centred cubic lattice (fcc) with almost identical metallic radii and chemical similarity, silver and gold represent a classical system for alloys ("electrum") with unlimited miscibility.[12, 15, 16] Alloyed silver-gold nanoparticles can be prepared by different methods like wet-chemical synthesis ("bottom-up"),[17-21] often leading to a gradient structure (gold-rich core and silver-rich shell),[22, 23] or laser ablation ("top-down"), leading to a homogeneous distribution of the elements inside each particle.[24] Theoretical considerations,[12] although not without controversy,[25, 26] predict a segregation of silver to the surface of alloyed silver-gold nanoparticles.

Nanoparticles and nanofilms usually contain smaller domains (crystallites, grains) with corresponding grain boundaries.[27-31] In nanoalloys, an inhomogeneous atom distribution leads to a high concentration of defects and a contraction of the unit cell.[23] Annealing can lead to structural

healing, i.e. the reduction of the defect concentration and internal stress. Here, we show the effect of temperature on lattice parameters, the crystallite size, and microstrain of pure silver, pure gold, and alloyed silver-gold nanoparticles with a narrow particle size distribution produced by wet-chemical co-reduction. We also address the question of the elemental distribution inside the nanoparticles after thermal treatment.

Results and discussion

Monometallic Ag and Au and bimetallic AgAu nanoparticles were synthesized by co-reduction with citrate and tannic acid in water and colloidal stabilization with poly(N-vinylpyrrolidone) (PVP).[22, 23, 32] They were characterized by elemental analysis (AAS), UV-vis spectroscopy, and transmission electron microscopy (TEM). In general, the particle size distribution as determined by TEM was narrow. The hydrodynamic diameter (solid particle core with the hydrated layer of the colloidal stabilizer PVP) of the water-dispersed nanoparticles was determined by differential centrifugal sedimentation (DCS). All analytical characterization data are summarized in Table 1.

Table 1: Compositional and structural data of PVP-coated AgAu nanoparticles, including nanoparticles of pure gold and silver. Standard deviations of the last digits are given in parentheses.

Nominal composition according to synthesis parameters Ag:Au / mol%:mol%	Analytical composition according to AAS Ag:Au / mol%:mol%	*d*(DCS) / nm	*d*(TEM) / nm	UV absorption maximum / nm
Au	0:100	8.2(8)	6.2(9)	523
10:90 = Ag10Au90	12:88	7.2(6)	-	512
20:80 = Ag20Au80	25:75	7.0(6)	-	505
30:70 = Ag30Au70	34:66	5.6(6)	-	505
40:60 = Ag40Au60	45:55	8.3(7)	7.9(8)	490
50:50 = Ag50Au50	62:38	6.7(6)	-	470
60:40 = Ag60Au40	64:36	8.3(6)	-	454
70:30 = Ag70Au30	74:26	7.2(5)	-	439
80:20 = Ag80Au20	83:17	8.7(9)	-	430
90:10 = Ag90Au10	90:10	7.8(6)	-	418
Ag	100:0	35(4)	31(4)	421

The elemental composition of bimetallic nanoparticles by atomic absorption spectroscopy was in good agreement with the nominal composition. The analytically determined compositions from AAS were used as input for the XRD analyses (Rietveld refinement). All particles were monodisperse with an average diameter of about 7 nm, except for pure silver nanoparticles that were significantly larger (35 nm). All nanoparticles were colloidally stable in water and did not agglomerate. In good agreement with the DCS results, the UV-vis spectra showed one narrow plasmon resonance peak, corroborating the monodisperse particle size distribution. The absorption

maxima of bimetallic AgAu nanoparticles were between the absorption maxima of pure Ag and Au nanoparticles and changed continuously with the Ag:Au molar ratio as expected.[23, 33]

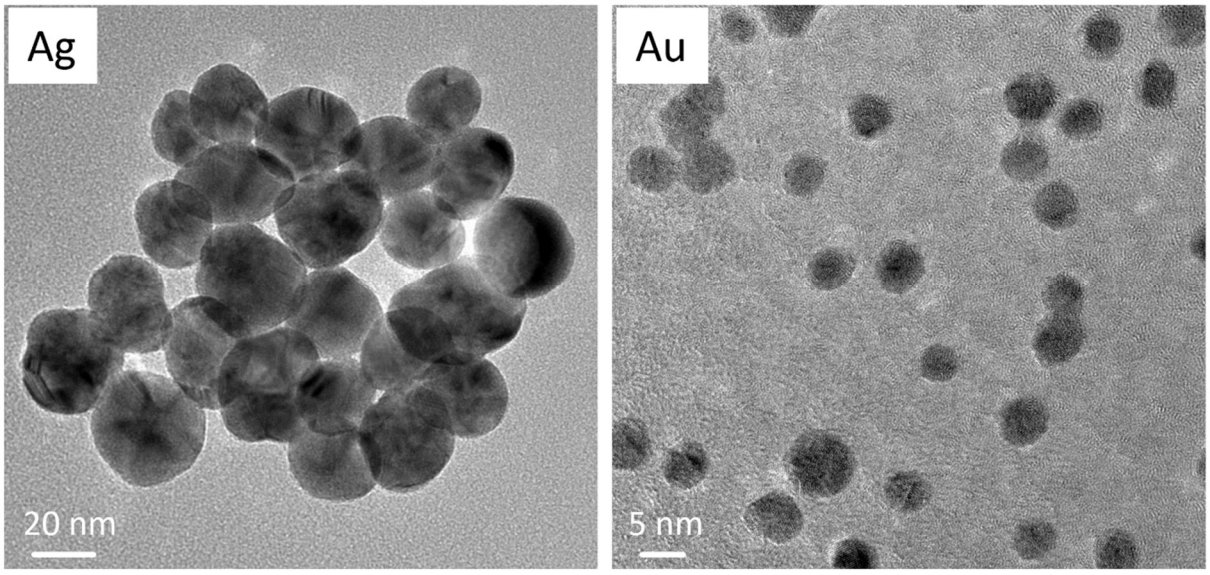

Figure 1: TEM images of silver nanoparticles (**left**) and gold nanoparticles (**right**) with a diameter of 35 and 7 to 9 nm, respectively.

Transmission electron microscopy showed spherical and monodisperse nanoparticles with a size of about 7 to 9 nm for Au nanoparticles (Figure 1), alloyed Ag40Au60 nanoparticles (Figure 9), and 35 nm for Ag nanoparticles (Figure 1), with clearly visible domains in the larger Ag nanoparticles. The particle size from TEM agreed well with the DCS results (Table 1).

The crystallographic properties of the nanoparticles were investigated by X-ray powder diffraction, followed by Rietveld refinement.[34] The calculated crystallite size of silver and alloyed nanoparticles was about one third of the average diameter from DCS and TEM (Tables 1 and 3), indicating a polycrystalline (twinned) ultrastructure.[28, 35] On the other hand, the crystallite size of gold nanoparticles was comparable with the particle size, indicating single-domain particles.

Twinned small nanoparticles (3-7 nm) with grain boundaries and an inhomogeneous elemental distribution contain an increased number of defects[36] and as a consequence, their physicochemical properties (i.e. surface energy and melting temperature) will change.[37-39] These atomic defects also lead to an increased microstrain ε[23, 40] due to the interaction between adjacent grains in such twinned nanostructures.[41] Both crystallite size *CS* and microstrain ε can be derived from X-ray diffraction peak broadening, with a greater pronouncement of the crystallite size at smaller angles and of the microstrain at larger angles.[42]

For *in-situ* X-ray diffraction, the samples were heated to 850 °C and then cooled to ambient temperature. The thermally-induced stress relaxation in these nanoparticles was elucidated by a detailed analysis of the diffraction data as comprised in Tables 2 and 3. Based on comprehensive Rietveld refinement, the lattice parameter *a*, the crystallite size *CS*, and the microstrain ε were computed for each sample at each temperature.

Table 2: Lattice parameter *a* of all nanoparticles at different temperatures determined by *in-situ* X-ray powder diffraction. In a few cases, the lattice parameter could not be safely determined due to weak reflection peaks. Standard deviations of the last digits are given in parentheses.

Ag: Au	*a* / Å (25 °C)	*a* / Å (150 °C)	*a* / Å (250 °C)	*a* / Å (400 °C)	*a* / Å (550 °C)	*a* / Å (700 °C)	*a* / Å (25 °C; after 850 °C)
Au	4.076(2)	4.083(2)	4.090(2)	4.100(2)	4.110(2)	4.122(1)	4.078(1)
10:90	-	4.078(6)	4.090(4)	4.099(4)	4.109(3)	4.123(2)	4.078(1)
20:80	4.062(6)	4.076(4)	4.089(3)	4.101(2)	4.110(2)	4.123(2)	4.078(1)
30:70	4.047(6)	4.062(6)	4.084(4)	4.097(4)	4.112(4)	4.124(2)	4.079(1)
40:60	4.050(6)	4.065(6)	4.089(4)	4.101(3)	4.112(2)	4.126(2)	4.079(1)
50:50	4.049(2)	4.071(2)	4.092(2)	4.103(2)	4.115(2)	-	4.078(1)
60:40	-	4.075(6)	4.095(3)	4.105(3)	4.117(2)	4.131(2)	4.079(1)
70:30	4.068(6)	4.082(6)	4.095(3)	4.108(2)	4.120(2)	4.135(2)	4.078(1)
80:20	4.070(4)	4.080(4)	4.098(2)	-	4.126(2)	4.141(1)	4.079(1)
90:10	4.080(4)	4.088(4)	4.101(2)	4.116(2)	4.129(1)	4.143(1)	4.079(1)
Ag	4.087(2)	4.098(2)	4.106(2)	4.119(2)	4.132(1)	4.148(1)	4.085(1)

Table 3: Crystallite size (*CS*) of all nanoparticles at different temperatures determined by *in-situ* X-ray powder diffraction. In a few cases, the crystallite size could not be determined due to weak reflection peaks. Standard deviations of the last digits are given in parentheses.

Ag: Au	*CS* / nm (25 °C)	*CS* / nm (150 °C)	*CS* / nm (250 °C)	*CS* / nm (400 °C)	*CS* / nm (550 °C)	*CS* / nm (700 °C)	*CS* / nm (25 °C; after 850 °C)
Au	5.0(15)	5.5(10)	7.4(5)	8.2(5)	9.2(5)	10.3(5)	12(1)
10:90	-	3(1)	9(1)	11(1)	12(1)	14(1)	33(1)
20:80	3.0(15)	4(1)	7(1)	9(1)	10(1)	10(1)	14(1)
30:70	3.4(15)	4(1)	4(1)	4(1)	4(1)	5(1)	14(1)
40:60	3.0(15)	3(1)	7(1)	9(1)	9(1)	11(1)	17(1)
50:50	3.1(15)	4(1)	10(1)	13(1)	15(1)	-	17(1)
60:40	-	4(2)	9(1)	12(1)	14(1)	15(1)	25(1)
70:30	3.0(15)	8(1)	11(1)	15(1)	17(1)	18(1)	40(2)
80:20	4(1)	3(1)	9(1)	-	25(3)	40(4)	50(5)
90:10	7(1)	9(1)	20(3)	50(5)	77(2)	100(5)	125(10)
Ag	10(1)	10(1)	12(1)	18(2)	40(6)	115(10)	-

X-ray powder diffraction showed three diffraction peaks of the AgAu fcc phase, i.e. (111), (200), and (220), together with peaks of the reference material LaB_6 and of the tantalum sample holder (Figure 2). With increasing temperature, two major effects occurred: The expected shift of the peaks to smaller 2θ values due to thermal expansion and peak narrowing due to recrystallization/crystallite size increase.

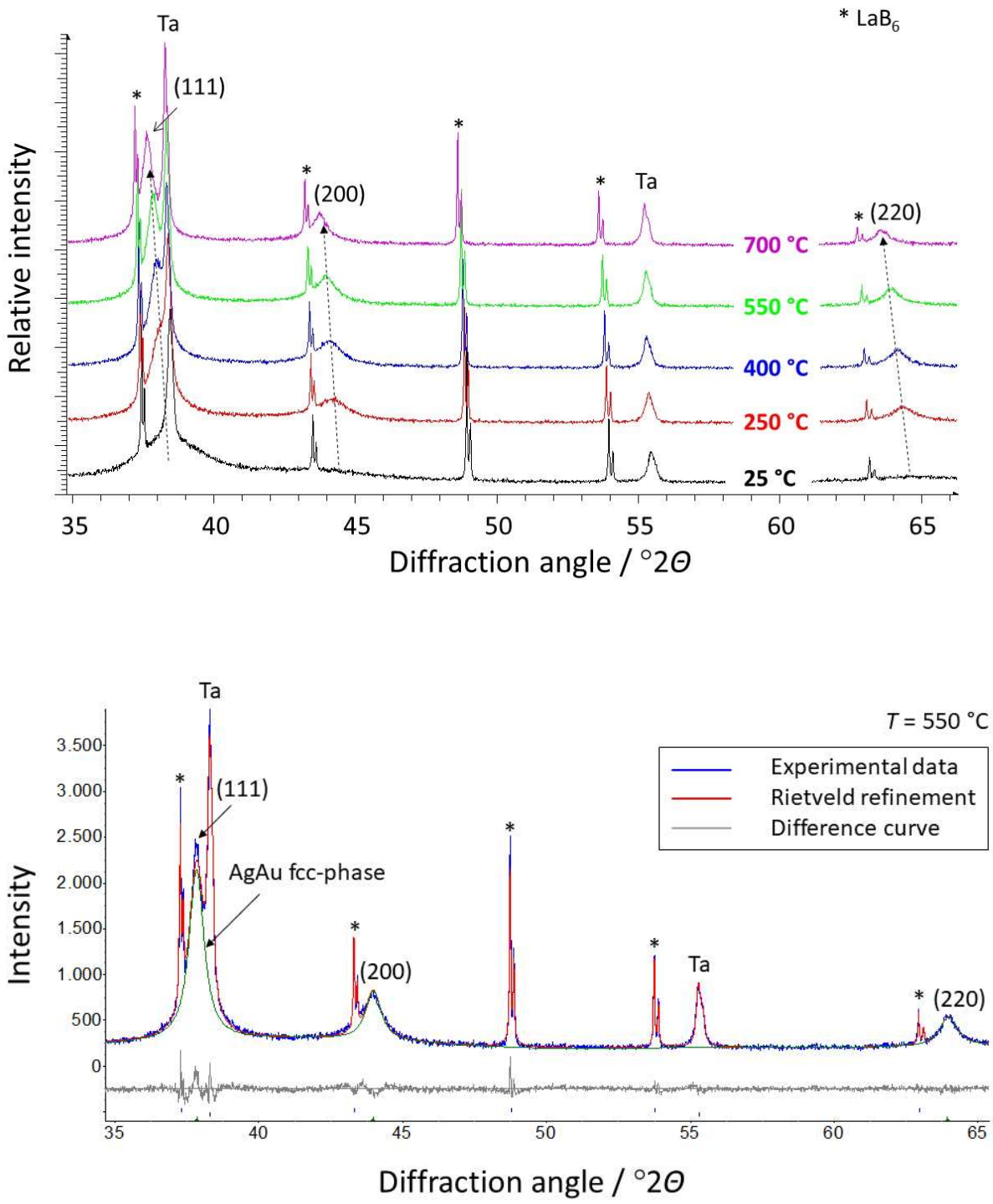

Figure 2: I*n-situ* X-ray diffractograms (**top**) with a representative Rietveld refinement (**bottom**, R_{wp}=6.2) of alloyed Ag50Au50 nanoparticles mixed with 15 wt% LaB_6 (labelled with *****; split peaks due Cu $K\alpha_{1,2}$ radiation) on a tantalum sample holder (labelled with **Ta**). Miller indices of the AgAu

fcc phase are indicated in parentheses. Note that the peaks of AgAu are still broader than those of LaB_6, even at 700 °C, i.e. the computed crystallite sizes are still reliable, although the experimental error increases (see Table 3).

The lattice parameters of alloyed AgAu nanoparticles showed a negative deviation from Vegard's law with the largest extent at the 50:50 composition (Figure 3). This deviation continuously decreased with increasing temperature to about one third (about 0.2%) that is comparable to bulk materials of the same composition.[43] This indicates a thermally induced structural relaxation of the AgAu nanoparticles as it is characteristic for metals during heat treatment.[44] This relaxation occurred between 150 and 250 °C (Figure 4). Notably, nanoparticles of pure silver and gold did not show a thermal relaxation because only little stress was present before. The structural relaxation was irreversible and persisted after cooling to room temperature.

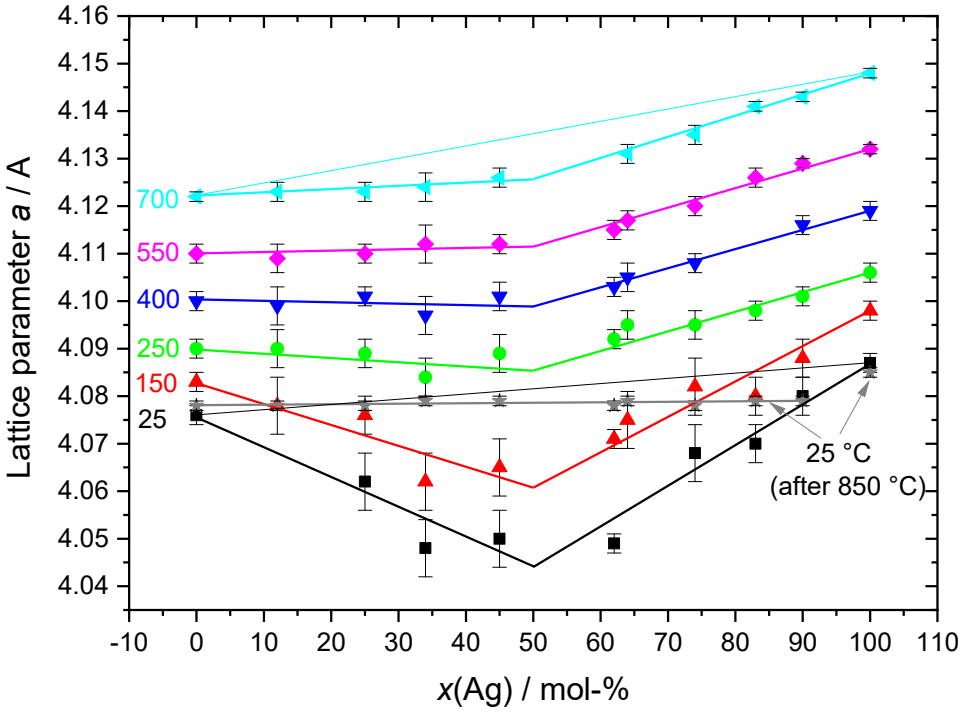

Figure 3: Lattice parameters of AgAu nanoparticles by *in-situ* X-ray powder diffraction. The negative deviation from Vegard's law decreased with increasing temperature. After heating to 850 °C and subsequent cooling to 25 °C, the negative deviation from Vegard's rule had vanished, indicating an irreversible structural relaxation in the nanoparticles (grey line and grey data points).

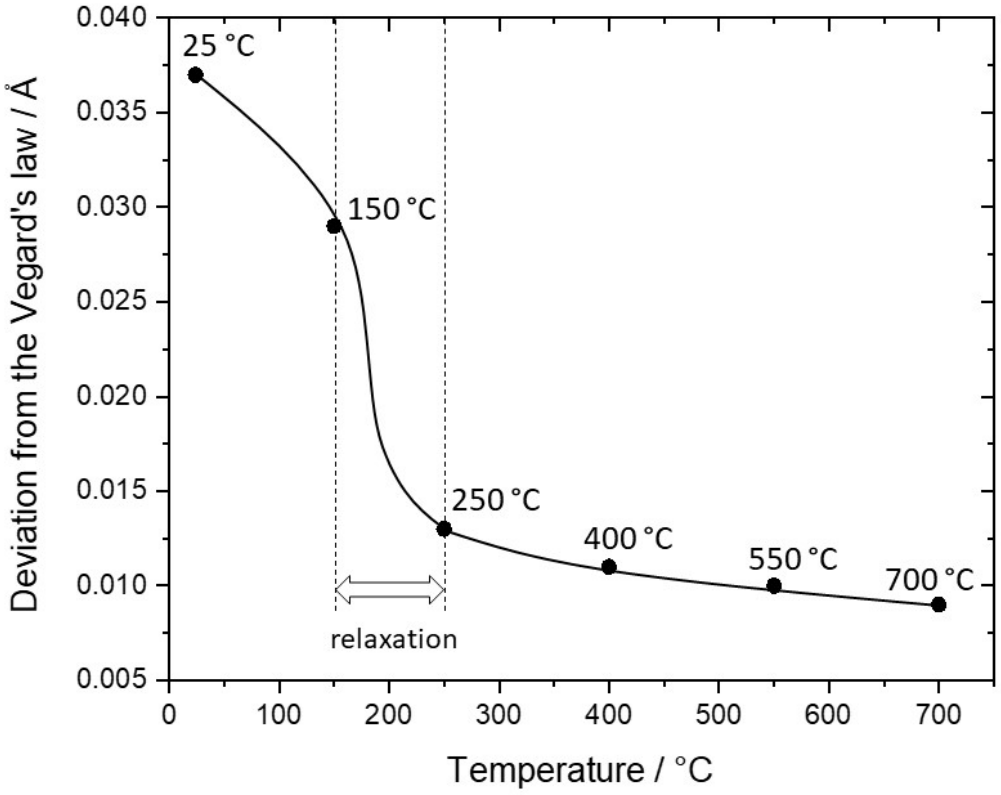

Figure 4: The negative deviation from Vegard's law (graphically derived from the data shown in Figure 3) in AgAu nanoparticles decreased with increasing temperature, especially in the region between 150-250 °C, indicating a structural relaxation.

The lattice parameters of pure silver and gold nanoparticles at room temperature, i.d. a(Ag)=4.087 Å and a(Au)=4.076 Å, were in good agreement with the bulk metals and corresponded well with the ICDD database, i.e. #4-0783 for silver: 4.0862 Å, and #4-0784 for gold: 4.0786 Å.[45] At 850 °C, silver had started to sublime at the applied high vacuum ($5 \cdot 10^{-3}$ Pa) in accordance with earlier reports,[46-49] therefore these data could not be interpreted.

The temperature-induced changes in the lattice parameter a lead us to the linear thermal expansion coefficient α_L. For pure silver and gold nanoparticles, this was in a good agreement with the parameters reported for the bulk metals, in agreement with the observation that these

nanoparticles did not show a measurable internal stress (Figure 5).[50] The lattice parameters of alloyed AgAu nanoparticles increased with increasing temperature but showed a clear jump between 150 and 250 °C that we associate with the structural relaxation described above. This was more pronounced for the silver-rich alloyed nanoparticles, especially with comparable amounts of silver and gold.

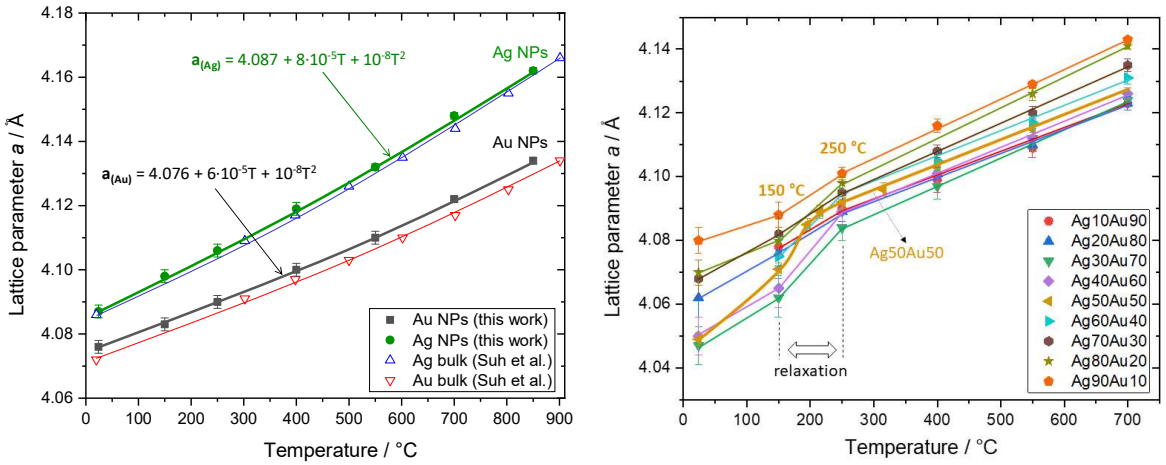

Figure 5: Temperature-dependent lattice parameter *a* of pure Ag and Au nanoparticles with polynomial fit curves (**left**) and of alloyed AgAu nanoparticles (**right**) with a jump at 200 °C as obtained by *in-situ* X-ray powder diffraction. The temperature-dependent lattice parameter *a* for bulk Ag and Au was taken from Suh et al.[50]

From the lattice parameters, the differential linear thermal expansion coefficient α_L was derived (Figure 6). This gives another illustration of the remarkable jump in *a* between 150 and 250 °C, leading to a maximum in α_L. This effect was observed for all alloyed nanoparticles but not for pure silver and gold nanoparticles. A similar non-linear behavior with a maximum in α_L was found by molecular dynamics (MD) simulations by Chu and Steeves for amorphous aluminum and titanium

during thermal recrystallization.[51] Negative thermal expansion coefficients were observed for Au nanospheres (4 nm) by Li et al.[52] and computed for metallic nanowires at low temperatures by Ho et al.[53]

Again, the thermal expansion coefficients for pure silver and gold nanoparticles were in good agreement with the reported data of the bulk materials (α_L(Au)=14·10^{-6} K^{-1} and α_L(Ag)= 19·10^{-6} K^{-1}).[54] Note that the thermal expansion coefficients of bulk gold and silver are temperature-dependent and increase to α_L(Au)=19.7·10^{-6} K^{-1} and α_L(Au)=27.1·10^{-6} K^{-1} at 827 °C, respectively.[55]

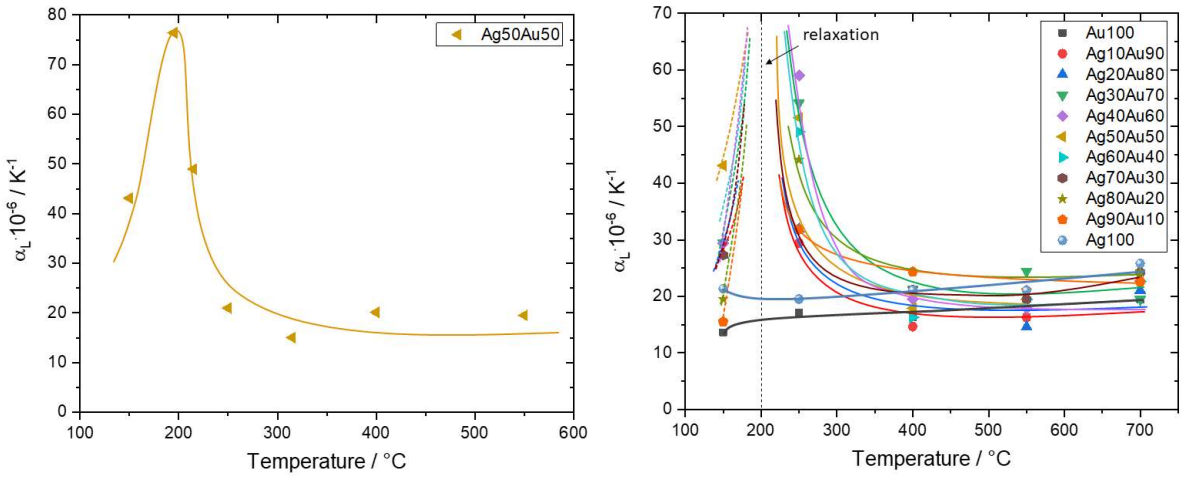

Figure 6: Linear thermal expansion coefficient α_L of alloyed Ag50Au50 nanoparticles (**left**) and of all investigated nanoparticles (**right**).

To investigate the temperature effect on the microstrain ε and on the crystallite size of the alloyed silver-gold nanoparticles, the diffraction data were analyzed in more detail (Table 3). Figure 7 shows the results for pure silver and gold nanoparticles and for alloyed Ag50Au50 nanoparticles, based on Williamson-Hall plots. The microstrain significantly decreased in all cases in the

temperature range of 150 to 250 °C, confirming the structural relaxation that was accompanied by the lattice expansion. The crystallite size showed a different trend. There was a strong jump between 150 and 250 °C for Ag50Au50 nanoparticles and a much less pronounced jump for pure gold nanoparticles. For silver nanoparticles, no jump but just an exponential increase in the crystallite size was observed, starting around 250 °C.

The jump-like discontinuity for Ag50Au50 nanoparticles was expected, but it is surprising that a similar behavior was observed for pure gold nanoparticles that did not show such a discontinuity in the thermal lattice expansion. The relaxation effect was least pronounced in silver, probably also due to the initially larger particles in the case of silver (Table 1). Similar results were found for all other alloyed nanoparticles (Figure 8). The added reference material LaB_6 did not show any thermal change except for the thermal expansion which was determined to $5.39 \cdot 10^{-6}$ K^{-1} in good agreement with the data reported by Chantler et al. ($5.42 \cdot 10^{-6}$ K^{-1}).[56] This also indicates a reasonable temperature calibration of the heating device used here.

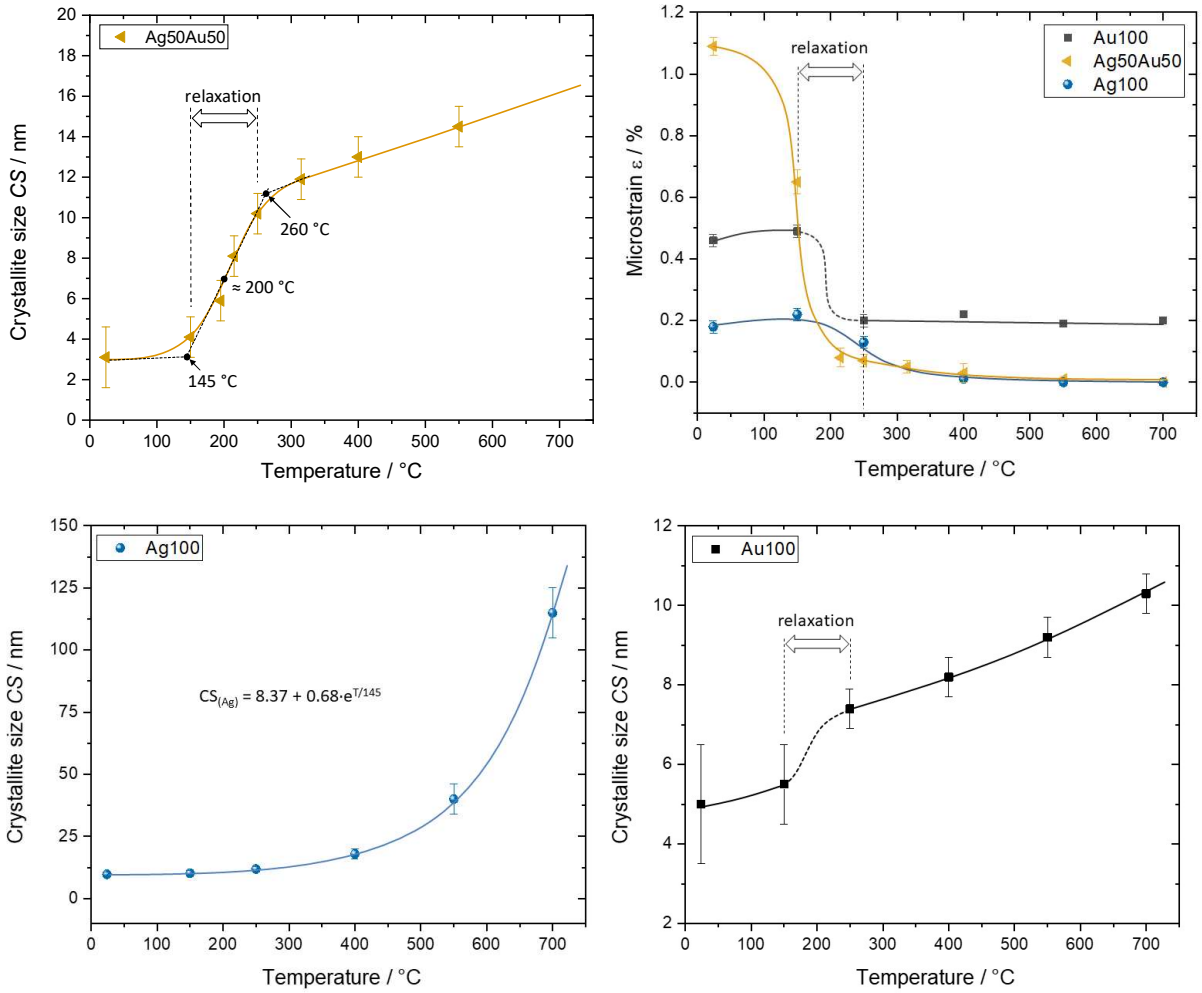

Figure 7: Temperature-dependent crystallite size of alloyed Ag50Au50 nanoparticles (**top left**) and pure Ag and Au nanoparticles (**bottom**), and microstrain of Ag50Au50 and pure Ag and Au nanoparticles (**top right**) with a drop between 150 and 250 °C as determined by *in-situ* X-ray powder diffraction.

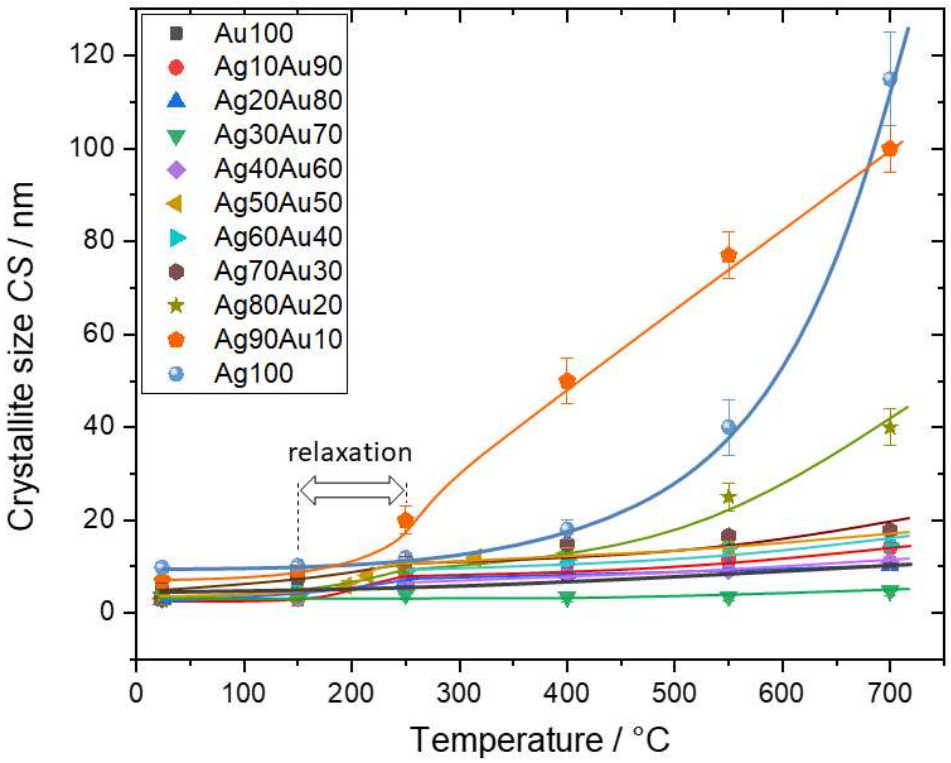

Figure 8: Crystallite size in alloyed AgAu nanoparticles as obtained by *in-situ* X-ray powder diffraction as function of composition and temperature.

The metal atoms are clearly mobile inside the nanoparticles above 150 °C. This is supported by reports by Rahman et al.[57] and Tomizuka et al.[58] who described the exponential increase in the self-diffusion coefficient of silver. Sadovnikov found a similar increase of the crystallite size with an exponential dependence with a simultaneous decrease of microstrain during vacuum annealing of Ag_2S nanopowders.[59] Song et al. reported an abrupt particle size increase in silver, gold, and AgAu nanoparticles (4 to 10 nm diameter) at 150 °C by *in-situ* X-ray diffraction in a limited angular region.[60] It is an important question to ask whether there is organic material inside the metallic nanoparticle that induces strain and thermal effects as observed for biominerals and mesocrystals.[61-63] This would apply to the polymer PVP. From earlier studies of gold nanoparticles

obtained by very similar syntheses, we know that the citrate content is about 3 wt% and the PVP content after ligand exchange is about 4-6 wt%.[64] Because PVP was added after the primary formation of the nanoparticles by reduction with citrate/tannic acid, it is reasonable to assume that the PVP was located on the nanoparticle surface and not inside. From the TEM images, there is no indication that organic material is occluded inside the nanoparticles, but unfortunately, there is no available method to exclude its presence with high reliability.

The nanoalloy Ag40Au60 was examined by HAADF-STEM and EDX after heating to 850 °C in the diffractometer and compared to the untreated nanoparticles (Figure 9). The original Ag40Au60 nanoparticles consisted of a gold-rich core and a silver-rich shell as observed earlier.[22, 23] In good agreement with the crystallite size by X-ray diffraction, domains with a size of about 4 nm were observed. After heating to 850 °C, the crystallite size had significantly increased and again agreed well with the X-ray diffraction results (13 nm). The particles were still spherical after heating with a slight increase in diameter. The particles had not melted, in good agreement with predictions by Guisbiers et al. on AgAu nanoalloys of different shape with a diameter of 10 nm.[12] EDX analysis in the TEM showed that before heating, the average molar ratio Au:Ag was 0.6(1) : 1. After heating the average molar ratio Au:Ag was 1.9(3) : 1. Thus, silver had clearly vanished. Although the chemical composition of the particles had changed to some extent, it is clear that the heat treatment caused a redistribution of Ag and Au atoms inside the nanoparticle towards a homogeneous alloy which obviously is thermodynamically favorable at 850 °C. Notably, this contrasts computations by Guisbiers et al. where a segregation of silver to the AgAu nanoparticle surface was predicted but not experimentally demonstrated.[12] It is important to point out that the organic shell (PVP) had already vanished at this temperature and that the annealing was performed in vacuum, therefore metal-ligand effects and solvent effects at the surface[12, 65-68] can be excluded.

It is unlikely that the elemental distribution present at 850 °C changed during the rapid cooling at the end of the annealing phase, therefore we are confident that we see a "frozen" snapshot of the equilibrium state at 850 °C.

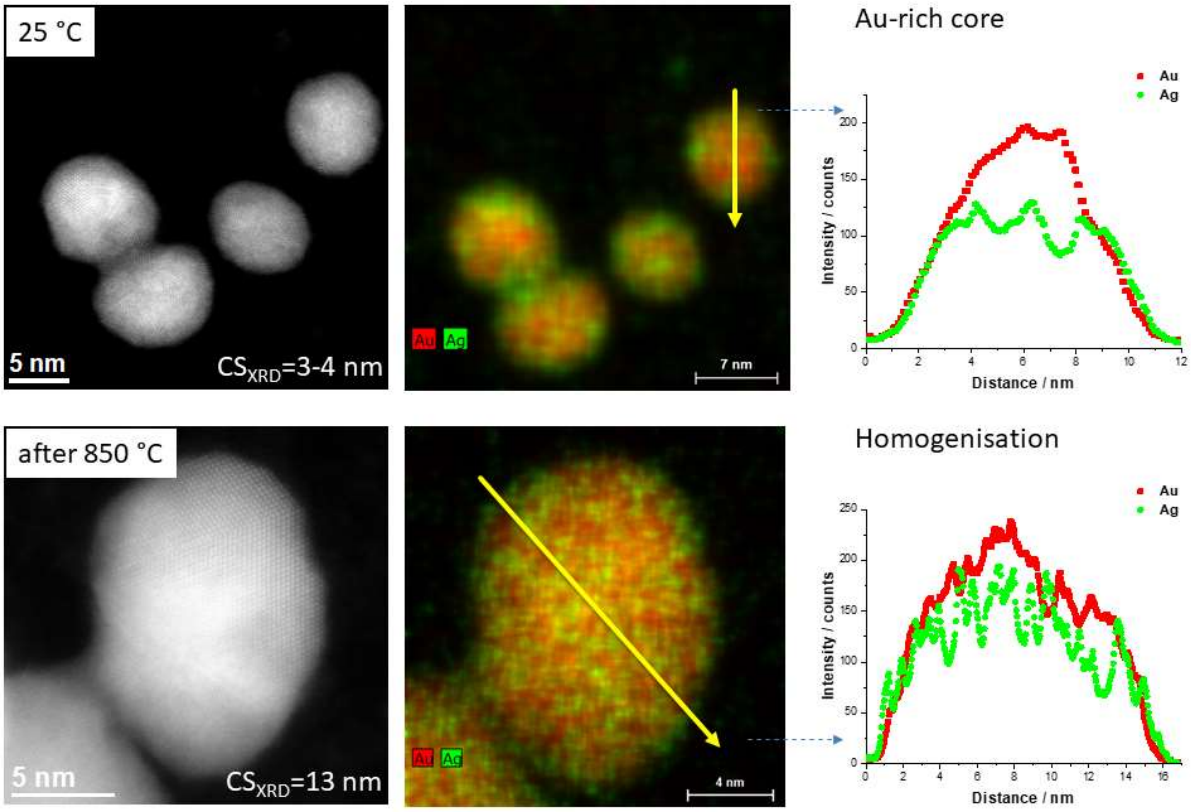

Figure 9: HAADF-STEM images with corresponding EDX map of Ag40Au60 nanoparticles before (**top**) and after *in-situ* X-ray diffraction at 850 °C (**bottom**).

Conclusions

Alloyed nanoparticles of silver and gold with a typical diameter of 6-8 nm have a gold-rich core and a silver-rich shell after wet-chemical synthesis. They also contain numerous defects and several crystalline domains. The thermal relaxation starts already at 150 °C in a discontinuous process that is mostly finished at 250 °C. By thermal relaxation, the microstrain inside the particles

considerably decreases due to merging of the individual crystalline domains, thus reducing the internal defect concentration. The internal stress was also visible as a remarkable negative deviation from Vegard's law. After heating to 250 °C, this deviation had also vanished. We conclude that the metal atoms have a considerable mobility inside the nanoparticles as no primary particle growth was observed up to 850 °C. After heating to 850 °C, the internal elemental distribution was homogeneous within now mostly single-crystalline nanoparticles, showing that a homogeneous elemental distribution is thermodynamically favorable at 850 °C.

Materials and Methods

Chemicals

For the nanoparticle syntheses, we used poly(N-vinyl pyrrolidone) (PVP K 30, Povidon 30; Sigma Aldrich, p.a., $M = 40{,}000$ g mol^{-1}), trisodium citrate dihydrate (AppliChem, p.a.), and tannic acid (Acros, 95%). Aqueous solutions of tetrachloridoauric acid (gold powder, Alfa Aesar 99.96+%, dissolved in *aqua regia*) and silver nitrate (Carl Roth, > 99.9%) were applied as ionic precursor compounds. Ultrapure water (Purelab ultra instrument from ELGA) was used in all experiments. Before using, all glassware was cleaned with boiling *aqua regia*.

Synthesis of nanoparticles

The synthesis was performed as described earlier.[23, 32, 69] In the following, the synthesis is described for the silver-gold 50:50 mol% composition and a reaction volume of 300 mL. By variation of the relative precursor amounts, the other nanoparticle compositions can be obtained. To obtain a sufficient mass of nanoparticles for characterization and *in-situ* X-ray powder diffraction, three to seven upscaled syntheses (300 mL reaction volume) were performed for each

composition. The batches were pooled after DCS and UV-vis characterization had shown the sample homogeneity and purity of each synthetic batch.

1.5 mL silver nitrate (10 mM, 15 µmol) and 1.5 mL tetrachloridoauric acid (10 mM, 15 µmol) were added to 300 mL of degassed water which was heated to 100 °C. For reduction, 3 mL trisodium citrate dihydrate (132 mM, 400 µmol) were mixed with 1 mL tannic acid (5 mM, 30 µmol) and added rapidly under vigorous stirring to the reaction mixture. After five minutes, the oil bath was removed and quickly replaced by an ice bath. The particles were functionalized with 6 mL poly(N-vinylpyrrolidone) (90 mM, 540 µmol) by stirring overnight at ambient temperature. The purification was performed by twice ultracentrifugation at 20,000 rpm/29,400 g (silver nanoparticles) or 30,000 rpm/66,000 g (all gold-containing nanoparticles) for 30 min, followed by redispersion in ultrapure water.

The syntheses of the pure Ag and Au nanoparticles were performed accordingly.[70] The amounts of the precursors were 3 mL silver nitrate (10 mM, 30 µmol) and 3 mL tetrachloridoauric acid (10 mM, 30 µmol), respectively.

After purification, the nanoparticles were freeze-dried (31 Pa and -10 °C; Alpha 2-4 LSC instrument; Martin Christ Gefriertrocknungsanlagen GmbH, Osterode am Harz, Germany) and gently ground to a homogeneous powder.

Characterization

The silver and gold contents were determined by atomic absorption spectroscopy (AAS) with a Thermo Electron M-Series spectrometer (graphite tube furnace; analysis performed according to DIN EN ISO/IEC 17025:2005) after dissolving the particles in nitric acid or *aqua regia*, respectively. The measurement uncertainty in AAS was 7% for both metals (relative uncertainty,

e.g. for a composition of Ag10Au90 it was a silver content of 10±0.7% and a gold content of 90±6.3%.

Analytical disc centrifugation (differential centrifugal sedimentation; DCS) was performed with a CPS Instruments DC 24000 disc centrifuge (24,000 rpm). Two sucrose solutions (8 wt% and 24 wt%) formed a density gradient which was capped with 0.5 mL dodecane as stabilizing agent to increase the gradient lifetime. The calibration standard was a poly(vinyl chloride) (PVC) latex in water with a particle size of 483 nm provided by CPS Instruments. The calibration was carried out prior to each run. A sample volume of 100 µL was used.

Ultraviolet–visible spectroscopy (UV-vis) was performed with a Varian Cary 300 instrument from 200 to 800 nm with solvent background correction. Suprasil® cuvettes with a sample volume of 3 mL were used.

In-situ X-ray powder diffraction (XRD) was carried out on a Panalytical Empyrean instrument in Bragg-Brentano mode with Cu Kα radiation (1.54 Å; 40 kV, 40 mA) equipped with a high-temperature chamber HTK 16 (Anton Paar). The freeze-dried nanoparticles were mixed with about 15 wt% microcrystalline LaB_6 (standard reference material SRM 660b of NIST, a=4.15689 Å). The reference material LaB_6 was necessary for the instrumental correction at different temperatures in the Rietveld refinement performed with the program package TOPAS 4.2 (Bruker). The sample was placed on the tantalum strip heater. All samples were investigated in high vacuum (10^{-3} Pa) at different temperatures (24 up to 850 °C) from 25 to 80° 2Θ with a step size of 0.01° so that each individual diffractogram took 40 min. The heating rate between the individual isothermal steps was 10 K min^{-1}. After reaching each temperature, the temperature was kept constant for 10 min for thermal equilibration before the XRD measurement started.

The XRD measurements were carried out from 25 to 80° 2Θ where the main four reflection peaks of Ag/Au with intensities *I*(111)=100% at 38.1°2Θ, *I*(200)=41% at 44.3 °2Θ, *I*(220)=25% at 64.4 °2Θ and *I*(311)=26% at 77.5° 2Θ appear. This also included the 100% (110) peak of LaB_6 at 30.4°. The Rietveld refinement was done for the whole 2Θ range of 25 to 80°.

By Rietveld refinement, crystallite size, lattice parameters, and linear thermal expansion coefficients were determined. The patterns of elemental silver (#4-0783), gold (#4-0784), LaB_6 (#34-0427), and Ta (#4-0788) from the ICDD database were used as standards. The data were not $K_{\alpha 2}$-corrected. Crystallite size *CS* and microstrain ε were calculated by the Scherrer[71] and the Stokes and Wilson equations,[72] respectively:

$$CS = \frac{K \cdot \lambda}{FWHM \cdot cos\theta} \qquad \varepsilon = \frac{FWHM}{4 \cdot tan\theta}$$

with K a constant set to 0.89, λ the wavelength of the X-ray radiation, FWHM the full width at half maximum of the diffraction peaks in radians, and θ the diffraction angle. The differential linear thermal expansion coefficient α_L was calculated as follows:[73]

$$\alpha_L = \frac{(a_{T2} - a_{T1})}{a_{T1} \cdot (T2 - T1)}$$

with a_T the lattice parameter *a* at temperature *T*.

Transmission electron microscopy (TEM) was performed with a Philips CM20 microscope, operated at 200 kV. Scanning transmission electron microscopy (STEM) was performed with a Titan 80–200 "ChemiSTEM" microscope, equipped with a Cs-probe corrector (CEOS), a high-

angle annular dark field (HAADF) detector, and four symmetrical SDD detectors for the elemental mapping acquisition by energy-dispersive X-ray spectroscopy (EDX). The operating voltage was 200 kV. *Z*-Contrast conditions were achieved with a probe semi-angle of 25 mrad and an inner collection angle of the detector of 70 mrad.[74, 75] The particle size distribution was determined by counting at least 20 nanoparticles (all spherical) and computing the average diameter and the standard deviation.

Acknowledgements

The authors acknowledge financial support of this work by the Deutsche Forschungsgemeinschaft (DFG) in the projects EP 22/44-1 and HE 7192/2-1. We thank Kerstin Brauner and Robin Meya for experimental assistance.

References

1. Duran, N.; Duran, M.; de Jesus, M. B.; Seabra, A. B.; Favaro, W. J.; Nakazato, G., Silver nanoparticles: A new view on mechanistic aspects on antimicrobial activity. *Nanomedicine* **2016,** *12*, 789-799.
2. Wolfbeis, O. S., An overview of nanoparticles commonly used in fluorescent bioimaging. *Chem. Soc. Rev.* **2015,** *44*, 4743-4768.
3. Langer, J.; Novikov, S. M.; Liz-Marzán, L. M., Sensing using plasmonic nanostructures and nanoparticles. *Nanotechnology* **2015,** *26*, 322001.
4. Chernousova, S.; Epple, M., Silver as antibacterial agent: Ion, nanoparticle, metal. *Angew. Chem. Int. Ed.* **2013,** *52*, 1636-1653.
5. Vericat, C.; Vela, M. E.; Benitez, G.; Carro, P.; Salvarezza, R. C., Self-assembled monolayers of thiols and dithiols on gold: New challenges for a well-known system. *Chem. Soc. Rev.* **2010,** *39*, 1805-1834.
6. Cobley, C. M.; Chen, J. Y.; Cho, E. C.; Wang, L. V.; Xia, Y. N., Gold nanostructures: a class of multifunctional materials for biomedical applications. *Chem. Soc. Rev.* **2011,** *40*, 44-56.
7. Scaletti, F.; Hardie, J.; Lee, Y. W.; Luther, D. C.; Ray, M.; Rotello, V. M., Protein delivery into cells using inorganic nanoparticle-protein supramolecular assemblies. *Chem. Soc. Rev.* **2018,** *47*, 3421-3432.
8. Dykman, L. A.; Khlebtsov, N. G., Multifunctional gold-based nanocomposites for theranostics. *Biomaterials* **2016,** *108*, 13-34.

9. Stark, W. J., Nanoparticles in biological systems. *Angew. Chem. Int. Ed.* **2011,** *50*, 1242-1258.
10. Larguinho, M.; Baptista, P. V., Gold and silver nanoparticles for clinical diagnostics - From genomics to proteomics. *J Proteomics* **2012,** *75*, 2811-2823.
11. Schlücker, S., Surface-Enhanced Raman Spectroscopy: Concepts and Chemical Applications. *Angew. Chem. Int. Ed.* **2014,** *53*, 4756-4795.
12. Guisbiers, G.; Mendoza-Cruz, R.; Bazan-Diaz, L.; Velazquez-Salazar, J. J.; Mendoza-Perez, R.; Robledo-Torres, J. A.; Rodriguez-Lopez, J. L.; Montejano-Carrizales, J. M.; Whetten, R. L.; Jose-Yacaman, M., Electrum, the gold–silver alloy, from the bulk scale to the nanoscale: synthesis, properties, and segregation rules. *ACS Nano* **2016,** *10*, 188-198.
13. Taylor, U.; Tiedemann, D.; Rehbock, C.; Kues, W. A.; Barcikowski, S.; Rath, D., Influence of gold, silver and gold–silver alloy nanoparticles on germ cell function and embryo development. *Beilstein J. Nanotechnol.* **2015,** *6*, 651-664.
14. Hannemann, S.; Grunwaldt, J. D.; Krumeich, F.; Kappen, P.; Baiker, A., Electron microscopy and EXAFS studies on oxide-supported gold-silver nanoparticles prepared by flame spray pyrolysis. *Appl. Surf. Sci.* **2006,** *252* (22), 7862-7873.
15. Okamoto, H.; Massalski, T. B., The Ag-Au (silver-gold) system. *Bull. Alloy Phase Diagr.* **1983,** *4*.
16. Banerjee, S.; Liu, C. H.; Lee, J. D.; Kovyakh, A.; Grasmik, V.; Prymak, O.; Koenigsmann, C.; Liu, H.; Wang, L.; Abeykoon, A. M. M.; Wong, S. S.; Epple, M.; Murray, C. B.; Billinge, S. J. L., Improved models for metallic nanoparticle cores from atomic pair distribution function (PDF) analysis. *J. Phys. Chem. C* **2018,** *122*, 29498-29506.
17. Goudeli, E.; Pratsinis, S. E., Surface composition and crystallinity of coalescing silver–gold nanoparticles. *ACS Nano* **2017,** *11*, 11653-11660.
18. Girao, A. V.; Pinheiro, P. C.; Ferro, M.; Trindade, T., Tailoring gold and silver colloidal bimetallic nanoalloys towards SERS detection of rhodamine 6G. *RSC Adv.* **2017,** *7*, 15944-15951.
19. Plowman, B. J.; Sidhureddy, B.; Sokolov, S. V.; Young, N. P.; Chen, A.; Compton, R. G., Electrochemical behavior of gold–silver alloy nanoparticles. *ChemElectroChem* **2016,** *3*, 1039-1043.
20. Sotiriou, G. A.; Etterlin, G. D.; Spyrogianni, A.; Krumeich, F.; Leroux, J. C.; Pratsinis, S. E., Plasmonic biocompatible silver-gold alloyed nanoparticles. *Chem. Commun.* **2014,** *50*, 13559-13562.
21. Zhou, T. Y.; Lin, L. P.; Rong, M. C.; Jiang, Y. Q.; Chen, X., Silver-gold alloy nanoclusters as a fluorescence-enhanced probe for aluminum ion sensing. *Anal. Chem.* **2013,** *85*, 9839-9844.
22. Grasmik, V.; Rurainsky, C.; Loza, K.; Evers, M. V.; Prymak, O.; Heggen, M.; Tschulik, K.; Epple, M., Deciphering the surface composition and the internal structure of alloyed silver–gold nanoparticles. *Chem. Eur. J.* **2018,** *24*, 9051-9060.
23. Ristig, S.; Prymak, O.; Loza, K.; Gocyla, M.; Meyer-Zaika, W.; Heggen, M.; Raabe, D.; Epple, M., Nanostructure of wet-chemically prepared, polymer-stabilized silver–gold nanoalloys (6 nm) over the entire composition range. *J. Mater. Chem. B* **2015,** *3* (23), 4654-4662.
24. Prymak, O.; Jakobi, J.; Rehbock, C.; Epple, M.; Barcikowski, S., Crystallographic characterization of laser-generated, polymer-stabilized 4 nm silver-gold alloyed nanoparticles. *Mater. Chem. Phys.* **2018,** *207*, 442-450.
25. Guisbiers, G.; Mendoza-Cruz, R.; Bazan-Diaz, L.; Velazquez-Salazar, J. J.; Mendoza-Perez, R.; Robledo-Torres, J. A.; Rodriguez-Lopez, J. L.; Montejano-Carrizales, J. M.; Whetten,

R. L.; Jose-Yacaman, M., Response to "Comment on 'electrum, the gold-silver alloy, from the bulk scale to the nanoscale: Synthesis, properties, and segregation rules'". *ACS Nano* **2016,** *10*, 10620-10622.
26. Cui, M.; Lu, H.; Jiang, H.; Meng, X., Comment on "Electrum, the gold–silver alloy, from the bulk scale to the nanoscale: Synthesis, properties, and segregation rules". *ACS Nano* **2016,** *10*, 10618-10619.
27. Luo, X. M.; Zhang, G. P., Grain boundary instability dependent fatigue damage behavior in nanoscale gold films on flexible substrates. *Mater. Sci. Eng. A* **2017,** *702*, 81-86.
28. Banerjee, S.; Loza, K.; Meyer-Zaika, W.; Prymak, O.; Epple, M., Structural evolution of silver nanoparticles during wet-chemical synthesis. *Chem. Mater.* **2014,** *26*, 951-957.
29. Tagliazucca, V.; Schlichte, K.; Schuth, F.; Weidenthaler, C., Molybdenum-based catalysts for the decomposition of ammonia: In situ X-ray diffraction studies, microstructure, and catalytic properties. *J. Catal.* **2013,** *305*, 277-289.
30. Ulvestad, A.; Sasikumar, K.; Kim, J. W.; Harder, R.; Maxey, E.; Clark, J. N.; Narayanan, B.; Deshmukh, S. A.; Ferrier, N.; Mulvaney, P.; Sankaranarayanan, S.; Shpyrko, O. G., In situ 3D imaging of catalysis induced strain in gold nanoparticles. *J. Phys. Chem. Lett.* **2016,** *7* (15), 3008-3013.
31. Chen-Wiegart, Y. C. K.; Harder, R.; Dunand, D. C.; McNulty, I., Evolution of dealloying induced strain in nanoporous gold crystals. *Nanoscale* **2017,** *9*, 5686-5693.
32. Mahl, D.; Diendorf, J.; Ristig, S.; Greulich, C.; Li, Z. A.; Farle, M.; Koeller, M.; Epple, M., Silver, gold, and alloyed silver-gold nanoparticles: characterization and comparative cell-biologic action. *J. Nanopart. Res.* **2012,** *14*, 1153.
33. Tiedemann, D.; Taylor, U.; Rehbock, C.; Jakobi, J.; Klein, S.; Kues, W. A.; Barcikowski, S.; Rath, D., Reprotoxicity of gold, silver, and gold-silver alloy nanoparticles on mammalian gametes. *Analyst* **2014,** *139*, 931-942.
34. Weidenthaler, C., Pitfalls in the characterization of nanoporous and nanosized materials. *Nanoscale* **2011,** *3*, 792-810.
35. Helmlinger, J.; Prymak, O.; Loza, K.; Gocyla, M.; Heggen, M.; Epple, M., On the crystallography of silver nanoparticles with different shapes. *Cryst. Growth Des.* **2016,** *16*, 3677-3687.
36. Zhou, C.; Yu, J.; Qin, Y.; Zheng, J., Grain size effects in polycrystalline gold nanoparticles. *Nanoscale* **2012,** *4*, 4228-4233.
37. Schmid, G., Large clusters and colloids - metals in the embryonic state. *Chem. Rev.* **1992,** *92*, 1709-1727.
38. Homberger, M.; Simon, U., On the application potential of gold nanoparticles in nanoelectronics and biomedicine. *Phil. Trans. R. Soc. A* **2010,** *368*, 1405-1453.
39. Liang, T.; Zhou, D.; Wu, Z.; Shi, P., Size-dependent melting modes and behaviors of Ag nanoparticles: a molecular dynamics study. *Nanotechnology* **2017,** *28*, 485704.
40. Zhang, Q.; Qin, Q.; Luo, Q.; Wu, Z.; Liu, L.; Shen, B.; Hu, W., Microstructure and nanoindentation behavior of Cu composites reinforced with graphene nanoplatelets by electroless co-deposition technique. *Sci. Rep.* **2017,** *7*, 1338.
41. Cullity, B. D.; Stock, S. R., *Elements of X-ray diffraction*. 3rd Edition ed.; Prentice-Hall Inc.: 2001.
42. Klug, H. P.; Alexander, L. E., *X-ray diffraction procedures for polycrystalline and amorphous materials*. Wiley-Interscience: New York, 1974.

43. Lubarda, V. A., On the effective lattice parameter of binary alloys. *Mech. Mater.* **2003,** *35*, 53-68.
44. Fox, A., *Effect of Temperature on Stress Relaxation of Several Metallic Materials*. Springer: Boston, 1982; Vol. 28.
45. Swanson, H. E.; Tatge, E., Standard x-ray diffraction patterns. *J. Res. Natl. Bur. Stand.* **1951,** *46*, 318-327.
46. Ding, Y.; Fan, F. R.; Tian, Z. Q.; Wang, Z. L., Sublimation-induced shape evolution of silver cubes. *Small* **2009,** *5*, 2812-2815.
47. Chatterjee, B., Anisotropy of melting for cubic metals. *Nature* **1978,** *275*, 203-203.
48. Castro, T.; Reifenberger, R.; Choi, E.; Andres, R. P., Size-dependent melting temperature of individual nanometer-sized metallic clusters. *Phys. Rev. B* **1990,** *42*, 8548-8556.
49. Zhu, Y. F.; Lian, J. S.; Jiang, Q., Modeling of the melting point, Debye temperature, thermal expansion coefficient, and the specific heat of nanostructured materials. *J. Phys. Chem. C* **2009,** *113*, 16896-16900.
50. Suh, I. K.; Ohta, H.; Waseda, Y., High-temperature thermal expansion of six metallic elements measured by dilatation method and X-ray diffraction. *J. Mater. Sci.* **1988,** *23*, 757-760.
51. Chu, J. J.; Steeves, C. A., Thermal expansion and recrystallization of amorphous Al and Ti: A molecular dynamics study. *J. Non-Cryst. Solids* **2011,** *357*, 3765-3773.
52. Li, W. H.; Wu, S. Y.; Yang, C. C.; Lai, S. K.; Lee, K. C.; Huang, H. L.; Yang, H. D., Thermal contraction of Au nanoparticles. *Phys. Rev. Lett.* **2002,** *89*, 135504.
53. Ho, D. T.; Kwon, S. Y.; Park, H. S.; Kim, S. Y., Negative thermal expansion of ultrathin metal nanowires: A computational study. *Nano Lett.* **2017,** *17*, 5113-5118.
54. Cverna, F., ASM ready reference. Thermal properties of metals. ASM International: Materials Park, Ohio, 2002.
55. Eichenauer, W., *Specific Heat, Metallic Elements and Alloys*. IFI/Plenum: New York-Washington, 1971; Vol. 4, p 830.
56. Chantler, C. T.; Tran, C. Q.; Cookson, D. J., Precise measurement of the lattice spacing of LaB6 standard powder by the x-ray extended range technique using synchrotron radiation. *Phys. Rev. A* **2004,** *69*, 042101.
57. Rahman, T.; McCloy, J.; Ramana, C. V.; Panat, R., Structure, electrical characteristics, and high-temperature stability of aerosol jet printed silver nanoparticle films. *J. Appl. Phys.* **2016,** *120*, 075305.
58. Tomizuka, C. T.; Sonder, E., Self-diffusion in silver. *Phys. Rev.* **1956,** *103*, 1182-1184.
59. Sadovnikov, S. I.; Rempel, A. A.; Gusev, A. I., *Nanostructured lead, cadmium, and silver sulfides: Structure, non stoichiometry and properties*. Springer Series in Materials Science: 2018; Vol. 256
60. Song, J. M.; Chen, W. T.; Hsieh, K. H.; Kao, T. H.; Chen, I. G.; Chiu, S. J.; Lee, H. Y., An in situ study on the coalescence of monolayer-protected Au-Ag nanoparticle deposits upon heating. *Nanoscale Res. Lett.* **2014,** *9*, 11.
61. Frølich, S.; Sørensen, H. O.; Hakim, S. S.; Marin, F.; Stipp, S. L. S.; Birkedal, H., Smaller calcite lattice deformation caused by occluded organic material in coccoliths than in mollusk shell. *Cryst. Growth Des.* **2015,** *15*, 2761-2767.
62. Zolotoyabko, E., Anisotropic lattice distortions in biogenic minerals originated from strong atomic interactions at organic/inorganic interfaces. *Adv. Mater. Interfaces* **2017,** *4*, 1600189.
63. Sturm, E. V.; Cölfen, H., Mesocrystals: structural and morphogenetic aspects. *Chem. Soc. Rev.* **2016,** *45*, 5821-5833.

64. Rostek, A.; Mahl, D.; Epple, M., Chemical composition of surface-functionalized gold nanoparticles. *J. Nanopart. Res.* **2011,** *13*, 4809-4814.
65. McNamara, K.; Tofail, S. A., Nanosystems: the use of nanoalloys, metallic, bimetallic, and magnetic nanoparticles in biomedical applications. *Phys. Chem. Chem. Phys.* **2015,** *17*, 27981-27995.
66. Calvo, F., Thermodynamics of nanoalloys. *PhysChemChemPhys* **2015,** *17*, 27922-27939.
67. Cerbelaud, M.; Ferrando, R.; Barcaro, G.; Fortunelli, A., Optimization of chemical ordering in AgAu nanoalloys. *Phys. Chem. Chem. Phys.* **2011,** *13*, 10232-10240.
68. Ferrando, R.; Jellinek, J.; Johnston, R. L., Nanoalloys: from theory to applications of alloy clusters and nanoparticles. *Chem. Rev.* **2008,** *108*, 845-910.
69. Ristig, S.; Chernousova, S.; Meyer-Zaika, W.; Epple, M., Synthesis, characterization and in-vitro effects of 7 nm alloyed silver-gold nanoparticles. *Beilstein J. Nanotechnol.* **2015,** *6*, 1212-1220.
70. Rostek, A.; Breisch, M.; Pappert, K.; Loza, K.; Heggen, M.; Köller, M.; Sengstock, C.; Epple, M., Comparative biological effects of spherical noble metal nanoparticles (Rh, Pd, Ag, Pt, Au) with 4–8 nm diameter. *Beilstein J. Nanotechnol.* **2018,** *9*, 2763-2774.
71. Scherrer, P., Bestimmung der Größe und der inneren Struktur von Kolloidteilchen mittels Röntgenstrahlen. *Nachr. Ges. Wiss. Göttingen* **1918,** *2*, 98-100.
72. Stokes, A. R.; Wilson, A. J. C., The diffraction of X-rays by distorted crystal aggregates. *Proc. Phys. Soc. London* **1944,** *56*, 174-181.
73. Taylor, R. E., *CINDAS Data Series on Materials Properties. Thermal Expansion of Solids*. ASM International: 1998.
74. Barthel, J.; Houben, L.; Tillmann, K., FEI Titan G3 50-300 PICO. *J. Large-scale Res. Fac.* **2015,** *1*, A34.
75. Kovács, A.; Schierholz, R.; Tillmann, K., FEI Titan G2 80-200 CREWLEY. *J. Large-scale Res. Fac.* **2016,** *2*, A43.